Physics of the Solid State, Vol. 46, No. 7, 2004, pp. 1301–1310. Translated from Fizika Tverdogo Tela, Vol. 46, No. 7, 2004, pp. 1261–1270.

LATTICE DYNAMICS AND PHASE TRANSITIONS

Hydrostatic Pressure–Induced Phase Transitions in $RbMnCl_3$: Raman Spectra and Lattice Dynamics

A. N. Vtyurin*, S. V. Goryaĭnov, N. G. Zamkova*, V. I. Zinenko*, A. S. Krylov*, S. N. Krylova*, and A. D. Shefer***

**Kirensky Institute of Physics, Siberian Division, Russian Academy of Sciences, Akademgorodok, Krasnoyarsk, 660036 Russia*

e-mail: vtyurin@iph.krasn.ru

***Joint Institute of Geology, Geophysics, and Mineralogy, Siberian Division, Russian Academy of Sciences, pr. Nauki 3, Novosibirsk, 630090 Russia*

Received September 26, 2003

Abstract—Raman scattering spectra of $RbMnCl_3$ are measured at room temperature under high hydrostatic pressure. The results are interpreted based on first principles lattice dynamics calculations. The experimental data obtained correlate with the calculations in the low frequency domain but disagree slightly in the region of high-frequency vibrations. The transition from the hexagonal to the cubic perovskite phase observed earlier (near 0.7 GPa) was confirmed, and new transitions to lower symmetry distorted phases were discovered (at 1.1 and 5 GPa). © *2004 MAIK "Nauka/Interperiodica".*

1. INTRODUCTION

The $RbMnCl_3$ crystal belongs to the large family of perovskite-like structures with the general formula ABX_3. The smaller radius cations B (in this case, of manganese) surrounded by anions X form fairly rigid octahedral groups in these structures, with the larger radius cations A located in the voids between these groups. These octahedra can share corners to form a classical cubic perovskite lattice (*c*-type packing in Fig. 1a) or faces in the case of hexagonal structures (*h*-type packing in Fig. 1b). Most of the widely known oxygen-containing perovskites crystallize in the cubic packing, and their properties have been studied in considerable detail. Halogen-containing perovskites are capable of forming both cubic and hexagonal lattices, as well as mixed structural types consisting of combinations of these two types [1], as illustrated in Fig. 1c. These structures are exemplified by $RbMnX_3$ crystals, where X stands for a halogen. The fluoride $RbMnF_3$ has a cubic perovskite structure, the bromide $RbMnBr_3$ possesses a hexagonal structure, and the chloride $RbMnCl_3$ has a mixed structure (Fig. 1c) [1, 2]. The similarity in the chemical composition and structure of these crystals gives grounds to suggest that a change in the external conditions (temperature or pressure) may induce phase transitions between these structural types, which should inevitably manifest itself in anomalies in the lattice dynamics. Indeed, $RbMnCl_3$ exhibits a phase transition with decreasing temperature (which is accompanied by restoration of the soft mode in the Raman spectrum [3]), as well as another transition from the hexagonal to cubic structure at high temperatures and pressures. In [4], a fine-grained $RbMnCl_3$ powder was subjected to a hydrostatic pressure of above 0.7 GPa and annealed under pressure (for half an hour at 700°C), after which the cubic structure stabilized in this way was studied under normal conditions. In [5], the cubic structure was observed to form in a part of the sample volume at comparable temperatures and pressures. Although it was pointed out that the actual annealing temperature affects the pressure of the transition to the cubic phase only slightly, this transition has nevertheless not been observed at room temperature to date.

Recent theoretical studies of this group of crystals [6] performed in an *ab initio* approach [7] revealed that the hexagonal structure of $RbMnCl_3$ should become unstable with increasing hydrostatic pressure, with the cubic modification of the crystal becoming energetically preferable (the calculated pressure at which the hexagonal lattice should lose stability is about 1 GPa, which correlates well with the experimental value of 0.7 GPa). According to those calculations, the onset of instability of the hexagonal lattice should be attributed to the high polarizability of the halogen ion and the breakdown of the fine balance between the multipole contributions to the energy of the hexagonal structure. Considering that the difference between the calculated energies of the cubic and hexagonal $RbMnCl_3$ lattices is very small and depends on pressure only weakly, those calculations obviously require experimental verification, both to test the validity of this approach for calculating the ion interaction potential as a whole and,

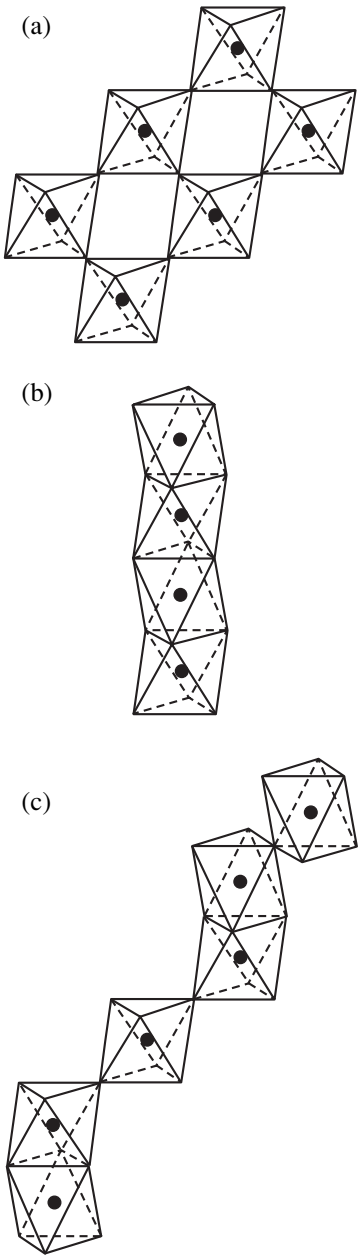

Fig. 1. Octahedral group packing in ABX_3 polytypes. (a) Cubic perovskite structure and (b) double-layer hexagonal and (c) six-layer hexagonal structures.

in particular, to look for the existence of a room temperature transition of the hexagonal to cubic structure in $RbMnCl_3$ under pressure.

This stimulated our present comparative experimental investigation of polarized Raman spectra in the hexagonal phase of $RbMnCl_3$ and of the vibrational spectrum calculated by the method proposed in [7] and by another technique similar to it [8] and a study of the effect of hydrostatic pressure on the Raman spectrum of this crystal.

2. STRUCTURE AND SYMMETRY OF THE CRYSTAL

The crystals intended for experimental study were Bridgman-grown in a quartz ampoule by multiple recrystallization. The grown bright red boules were 40 mm in diameter and up to 50 mm long and were inspected to select regions with no inclusions, crystallites, or other structural defects visible with a microscope. The samples fabricated for polarization measurements were rectangular parallelepipeds measuring $3 \times 4 \times 5$ mm, with two edges oriented along the *a* and *c* crystallographic axes. The orientation was performed using the x-ray technique to within $\pm 15'$ and using a polarization microscope; in the course of experiments conducted under normal conditions, the crystal orientation was checked periodically from the absence of birefringence in the sample and from the Rayleigh scattering background level. The techniques employed to grow the single crystals and prepare the samples are described in [3].

At room temperature, the structure of the crystal belongs to space group $P6_3/mmc$, $Z = 6$ [1, 9]. Each of the ions in the unit cell can occupy two symmetry-independent positions, with the five atomic coordinates not being fixed by crystal symmetry (Table 1). As follows both from experimental studies [9] and from calculations of the equilibrium crystal structure [6], the $MnCl_6$ octahedra differ slightly from the ideal shape; indeed, they are extended along the hexagonal axis.

The vibrational representation can be decomposed into irreducible representations at the center of the Brillouin zone for the hexagonal phase as

$$\begin{aligned}\Gamma &= 5A_{1g}(xx, yy, zz) + 6E_{1g}(xz, yz, zx, zy)\\ &+ 8E_{2g}(xx, yy, xy, yx) + A_{1u} + 7A_{2u} + 2B_{1u} + 6B_{2u}\\ &+ 9E_{1u} + 7E_{2u} + 2A_{2g} + 6B_{1g} + B_{2g},\end{aligned} \quad (1)$$

with the Raman tensor components in which the vibrational modes of the corresponding symmetry are active being shown in parentheses. While this result differs somewhat from the expression given in [3], it agrees with the number of vibrational degrees of freedom per unit cell and is in accord with [8].

One can write a similar expression for the cubic phase ($Pm3m$, $Z = 1$),

$$\Gamma = 4F_{1u} + F_{2u}. \quad (2)$$

This expression does not contain Raman active vibrations. As follows from a comparison of Eqs. (1) and (2), the selection rules for these structures are essentially different, which greatly simplifies their assignment by Raman spectroscopy.

3. EXPERIMENTAL TECHNIQUE AND RESULTS

3.1. Raman Scattering under Normal Conditions

The experiment under normal conditions was performed on a computerized DFS-24-based Raman spectrometer. The experimental techniques used, the design of the setup, and the data treatment chosen were described in considerable detail in [10]. Ar^+ laser polarized radiation served for pumping (500 mW, 514.5 nm).

We obtained spectra in four scattering geometries: $y(xx)z$ with the expected lines, according to Eq. (1), $5A_{1g} + 8E_{2g}$; $y(xy)z$ with $8E_{2g}$ lines, $y(xz)x$ with $6E_{1g}$ lines; and $y(zz)x$ with $5A_{1g}$ lines. The results obtained are displayed in Fig. 2.

The $y(xz)x$ and $y(zz)x$ components are seen to be substantially weaker than the others (the spectra are plotted on an arbitrary scale, but the drop in scattering intensity is evident from the deteriorating signal/noise ratio). Obviously enough, this is due to a strong anisotropy in the crystal susceptibility. Out of the five expected A_{1g} lines, only two, at 55 and 178 cm^{-1}, can be reliably detected in Fig. 2c. To search for the others, the spectra in Figs. 2a and 2b need to be compared. In comparison with Fig. 2b, Fig. 2a reveals a strong increase in intensity in the region of 260 cm^{-1} and a somewhat weaker, but still clearly pronounced increase near 138 cm^{-1}. The remaining maxima in Figs. 2a and 2b, namely, the maxima at 49, 60, 78, 154, 174, and 218 cm^{-1}, should be assigned to E_{2g}-type vibrations. Note that the strongest spectral line at 260 cm^{-1} also manifests itself in the *xy* component, although at a substantially lower intensity, which may be due to either sample misorientation or to the radiation becoming depolarized by defects in the crystal structure. The remaining, weakest component of the *xz* spectrum is shown in Fig. 2d. Out of the six expected E_{1g} lines, one sees reliably only the maxima at 55, 111, and 153 cm^{-1}, with a tentative identification of a weak line near 80 cm^{-1}; its intensity is, however, comparable to the background level.

3.2. Raman Scattering under Pressure

Room temperature experiments under high hydrostatic pressure (up to 9 GPa) were carried out on a diamond anvil setup similar to the one employed in [11, 12]; the chamber containing the sample was 0.25 mm in diameter and 0.1 mm in height. The pressure was determined to within 0.05 GPa from the luminescence band shift of ruby [12, 13], a microcrystal of which was placed near the nonoriented sample measuring 50–70 μm. The pressure-transmitting medium was a highly dehydrated mixture of ethyl and methyl alcohols. The Raman spectra were also excited by an Ar^+ laser (514.5 nm, 500 mW) and recorded with an OMARS 89 (Dilor) multichannel Raman spectrometer. Because of the small sample size and the strong diffuse scattering, only the high-frequency part of the spectrum (150–500 cm^{-1}) was recorded. Simultaneously, the domain structure and birefringence in the sample were observed with a polarization microscope.

Table 1. Positions of atoms in the six-layer hexagonal structure of $RbMnCl_3$ (in units of a_h = 7.1 Å, c_h = 19.0 Å [8])

Ion	Position	*x*	*y*	*z*
Rb1	2(*b*)	0	0	1/4
Rb2	4(*f*)	1/3	2/3	z_1
Mn1	2(*a*)	0	0	0
Mn2	2(*f*)	1/3	2/3	z_2
Cl1	6(*h*)	y_1	$2y_1$	1/4
Cl2	12(*k*)	y_1	$2y_2$	z_3

The transformation of the spectrum with pressure is shown in Fig. 3. The high-frequency part of the spectrum observed under normal pressure coincides with that shown in Fig. 2a; namely, one clearly sees a strong peak at 260 cm^{-1}, a weak maximum at 218 cm^{-1}, and an increase in intensity as the 154–174 cm^{-1} doublet is approached. A similar pattern (with a slight increase in the peak frequency) is observed when the pressure is increased to ~0.4 GPa, where the spectral intensity begins to gradually fall off. At the same time, the microscope reveals the appearance and growth of an optically isotropic region in the crystal. Note that the possible phase separation at the pressure-induced transition to the cubic phase was pointed out in [5]. At pressures above 0.75 GPa, there is no Raman scattering at all and the crystal becomes completely optically isotropic (with the exception of small regions on the surface, which may be due either to surface defects or to crystal interaction with the pressure-transmitting medium). This phase transition point agrees satisfactorily with the value of 1.1 GPa quoted in [6] and the transition pressure of 0.7 GPa reported in [4].

As the pressure increases above ~1.1 GPa, Raman scattering reappears, but its spectrum changes the pattern in that the 218 cm^{-1} line is absent and a doublet forms in its place in the region of 200 cm^{-1}. On the whole, the pattern of the spectrum (in this high-frequency part, which derives primarily from stretch vibrations of the bonds forming the octahedral groups) closely resembles that of the spectra of "cubic" perovskites after transition to the rhombohedrally distorted phase (see, e.g., [14]). As the pressure increases, the intensity of the Raman lines and their frequencies increase. At pressures near 5 GPa, the frequency growth rate increases, while the line intensities start to wane noticeably, which may indicate the onset of one more phase transition (Fig. 4). No other transient phenomena are observed in the spectra as the pressure is increased still more (up to 9.65 GPa). As the pressure is relieved, the crystal recovers its original state by passing through the same sequence of changes. Multiple transitions

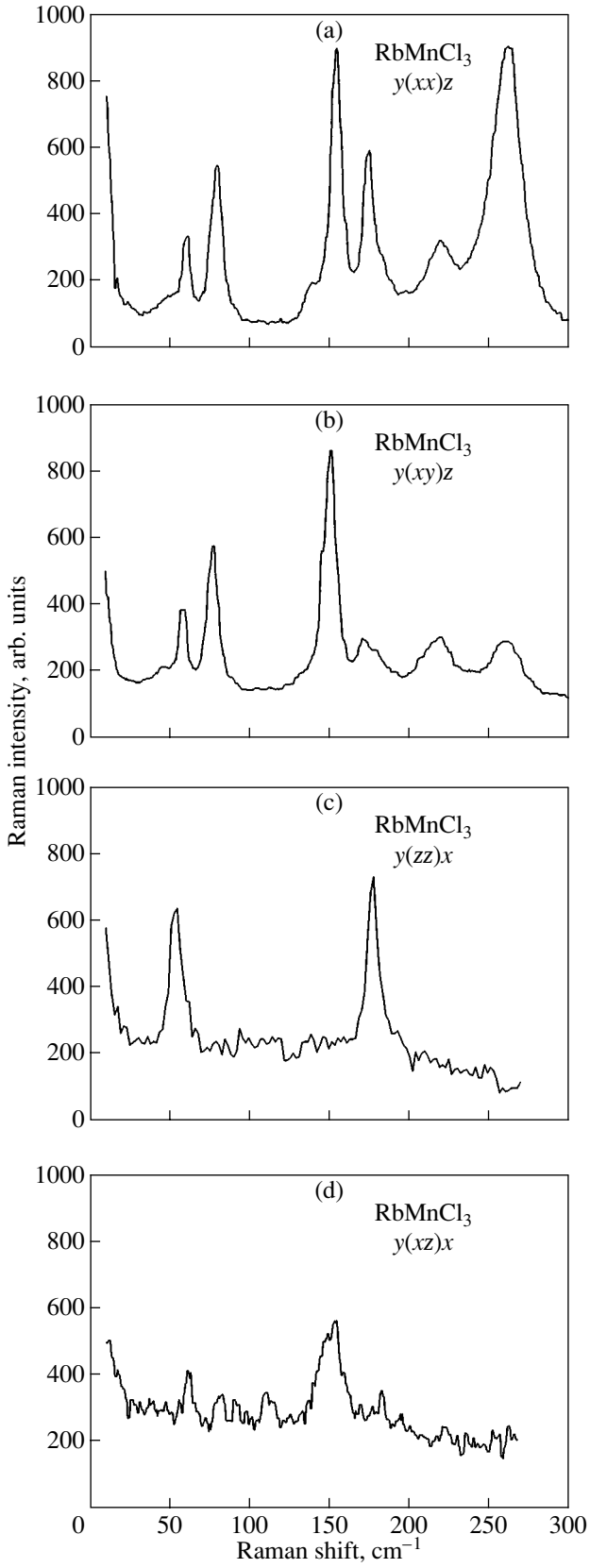

Fig. 2. Room-temperature polarized Raman spectra of $RbMnCl_3$ measured in different scattering geometries.

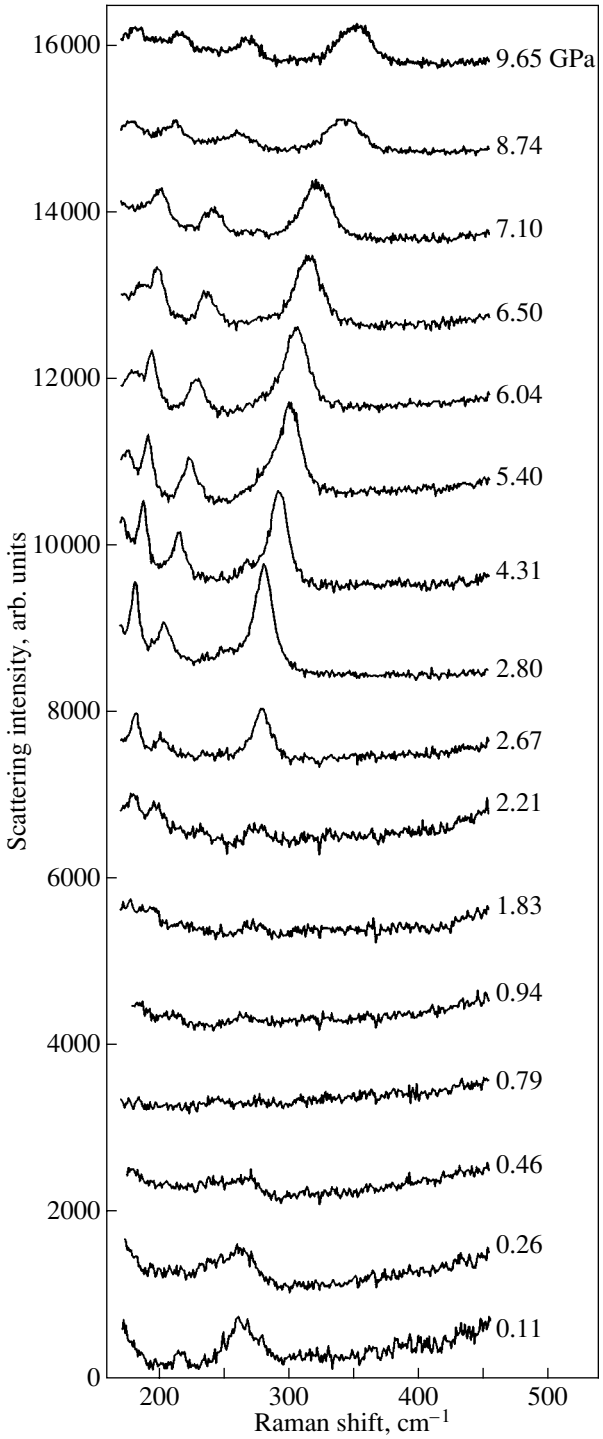

Fig. 3. Pressure-induced transformation of the high-frequency part of a Raman spectrum.

through the first detected point of transition from the hexagonal to the optically isotropic phase do not entail its displacement, nor are any hysteresis phenomena observed (within the measurement accuracy), in contrast with [4], where the annealed cubic phase persisted after the removal of pressure.

4. MODELING OF THE SPECTRUM

To calculate the vibrational spectrum, we used the Gordon–Kim model and took into account the ion electronic density distortion up to quadrupoles [7, 15]. The electronic density of the crystal in this model is represented as the sum of electronic densities of individual ions:

$$\rho_i(\mathbf{r}) = \sum_{l=0}^{2}\sum_{m=-l}^{l} \rho_i^{(l)}(r)Y_{lm}(\theta,\phi), \tag{3}$$

where $\rho_i^{(1)}$ and $\rho_i^{(2)}$ are the dipole and quadrupole components of the ion electronic density, respectively. The electronic density of an ion was calculated in terms of the Watson sphere, which describes the effect of the crystal environment [7, 15]:

$$V(\mathbf{r}) = \begin{cases} -Z/R_W, & r < R_W \\ -Z/r, & r > R_W \end{cases}, \tag{4}$$

where Z is the ion charge and R_W is the radius of the Watson sphere. The total crystal energy can be written as

$$E = E_0 + E_{d-d} + E_{q-q} + E_{d-q} + E_{\text{self}}, \tag{5}$$

where E_{self} is the sum of the ion self-energies,

$$E_0 = -\frac{1}{2}Z\hat{C}^{(0)}Z + \Phi^{(00)} \tag{6}$$

is the interaction energy of spherically symmetric ions, and

$$\begin{aligned} E_{d-d} &= \frac{1}{2}\mathbf{d}(\hat{\alpha}_d^{-1} + \hat{\Phi}^{(11)} - \hat{C}^{(2)})\mathbf{d} + \mathbf{d}(\hat{\Phi}^{(10)} - \hat{\mathbf{C}}^{(1)}Z), \\ E_{Q-Q} &= \frac{1}{2}\mathbf{Q}\left[\hat{\alpha}_Q^{-1} - \frac{1}{36}(\hat{\Phi}^{(22)} - \hat{\mathbf{C}}^{(4)})\right]\mathbf{Q} \\ &\quad - \frac{1}{6}\mathbf{Q}(\hat{\Phi}^{(20)} - \hat{\mathbf{C}}^{(2)}\mathbf{Z}), \\ E_{d-Q} &= -\frac{1}{6}\mathbf{Q}(\hat{\Phi}^{(21)} - \hat{\mathbf{C}}^{(3)})\mathbf{d} \end{aligned} \tag{7}$$

are the energies of the dipole–dipole, quadrupole–quadrupole, and dipole–quadrupole interactions, respectively; $\hat{\alpha}_d$ and $\hat{\alpha}_Q$ are the diagonal matrices of the dipole and quadrupole polarizabilities of single ions calculated by the Steinheimer method (for more details, see [7]). The short-range parts of the ion pair interactions $\Phi^{(ll')}$ are calculated in terms of the density functional theory as

$$\begin{aligned} \Phi_{ij}^{ll'} &= F(\rho_i^{(l)}(\mathbf{r}' - \mathbf{R}_i) + \rho_j^{(l')}(\mathbf{r} - \mathbf{R}_i)) \\ &\quad - F(\rho_i^{(l)}(\mathbf{r} - \mathbf{R}_i) - \rho_j^{(l')}(\mathbf{r} - \mathbf{R}_i)), \end{aligned} \tag{8}$$

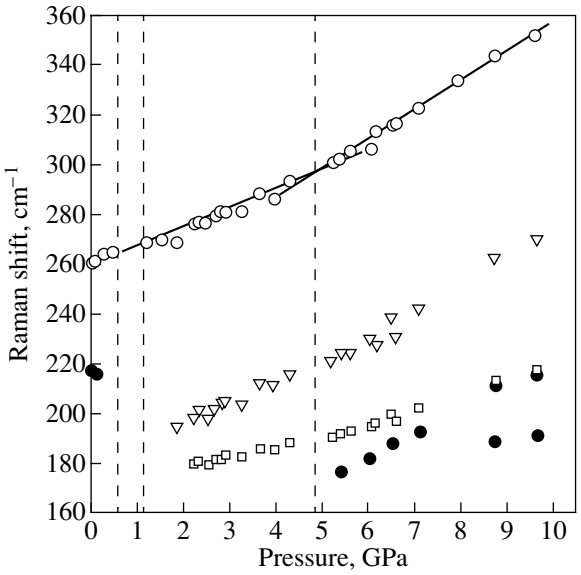

Fig. 4. Pressure dependences of the strongest spectral line frequencies. Dashed vertical lines indicate the tentative transition points, and solid straight lines are linear extrapolations.

and the long-range part of the interaction potential

$$C_{ij}^{(l+l')} = \nabla^{(l+l')}\frac{1}{|\mathbf{R}_{ij}|} \tag{9}$$

is calculated by Ewald's method. The fitting parameters of the structure (Table 1), as well as the dipole and quadrupole ion moments, were determined from the following energy minimum conditions:

$$\frac{\partial E}{\partial \mathbf{d}} = 0,$$

[whence it follows that

$$\begin{aligned} \mathbf{d} &= \hat{\mathbf{A}}[\hat{\Phi}^{(10)} - \hat{\mathbf{C}}^{(1)}\mathbf{Z} + \mathbf{Q}(\hat{\Phi}^{(21)} - \hat{\mathbf{C}}^{(3)})], \\ \hat{\mathbf{A}} &= (\hat{\alpha}_d^{-1} + \hat{\Phi}^{(11)} - \hat{\mathbf{C}}^{(2)})^{-1}, \end{aligned} \tag{10}$$

with **A** being a matrix that is the inverse of that of the dipole–dipole interaction in Eq. (7)] and

$$\frac{\partial E}{\partial \mathbf{Q}} = 0,$$

which yields the equation

$$\mathbf{Q} = \hat{\mathbf{B}}(\hat{\Phi}^{(20)} - \hat{\mathbf{C}}^{(2)} + \hat{\mathbf{A}}'),$$

where

$$\begin{aligned} \hat{\mathbf{B}} &= \left[\hat{\alpha}_Q^{-1} - \frac{1}{36}(\hat{\Phi}^{(22)} - \hat{\mathbf{C}}^{(4)})\right. \\ &\quad \left. + (\hat{\Phi}^{(21)} - \hat{\mathbf{C}}^{(3)})\hat{\mathbf{A}}(\hat{\Phi}^{(21)} - \hat{\mathbf{C}}^{(3)})^+\right]^{-1}, \\ \hat{\mathbf{A}}' &= (\hat{\Phi}^{(10)} - \hat{\mathbf{C}}^{(1)}\mathbf{Z})\hat{\mathbf{A}}(\hat{\Phi}^{(21)} - \hat{\mathbf{C}}^{(3)})^+. \end{aligned} \tag{11}$$

Note that the structural parameters calculated in this way are almost identical to the figures derived experimentally [8]. Equations (3)–(11) are discussed in more detail in [6].

To calculate the vibrational spectrum of a crystal, one has to take into account the dependence of its energy (5) on the displacements of ions from their equilibrium positions. The corresponding expression for the dynamic matrix, including the electronic polarizability of ions and their breathing modes in the crystal environment, can be written in the form (for a crystal of arbitrary symmetry) [7]

$$D_{\alpha\beta}(\mathbf{q}, jj') = \frac{\exp(-i\mathbf{q}\mathbf{X}_{jj'})}{\sqrt{M_j M_{j'}}}$$

$$\times\left\{\frac{1}{2}Z_j C^{(2)}_{\alpha\beta}(\mathbf{q}, jj')Z_{j'} + \tilde{D}^{\alpha\beta}_{RR}(\mathbf{q}, jj')\right. \quad (12)$$

$$\left. - \sum_{k,k'=1}^{N_a} \tilde{D}^{\alpha}_{RV}(\mathbf{q}, jk)\tilde{D}_{VV}(\mathbf{q}, kk')\tilde{D}^{\beta *}_{RV}(\mathbf{q}, j'k')\right\}.$$

The matrices entering Eq. (12) are defined as follows:

$$D^{\alpha\beta}_{RR}(\mathbf{q}, jj') = \Phi^{(00)}_{RR,\alpha\beta}(\mathbf{q}, jj')$$

$$- \sum_{\gamma\delta=1}^{3}\sum_{k,k'=1}^{N_a} [\Phi^{(01)}_{R,\alpha\gamma}(\mathbf{q}, jk) - C^{(2)}_{\alpha\gamma}(\mathbf{q}, jk)Z_k]$$

$$\times A_{\alpha\gamma}(\mathbf{q}, kk')[\Phi^{(01)}_{R,\beta\delta}(\mathbf{q}, k'j') - C^{(2)}_{\beta\delta}(\mathbf{q}, k'j')Z_{k'}],$$

$$A_{\alpha\beta}(\mathbf{q}, jj') = \left[\frac{\delta_{\alpha\beta}\delta_{jj'}}{\alpha_{d,j}} + \Phi^{(11)}_{\alpha\beta}(\mathbf{q}, jj') - C^{(2)}_{\alpha\beta}(\mathbf{q}, jj')\right],$$

$$D^{\alpha}_{RV}(\mathbf{q}, jj') = \Phi^{(00)}_{RV,\alpha}(\mathbf{q}, jj')$$

$$- \sum_{\gamma=1}^{3}\sum_{k,k'=1}^{N_a} \Phi^{(01)}_{R,\alpha}(\mathbf{q}, jk)A_{\alpha\gamma}(\mathbf{q}, kk')\Phi^{*(01)}_{V,\gamma}(\mathbf{q}, k'j'),$$

$$D_{VV}(\mathbf{q}, jj') = \Phi^{(00)}_{VV}(\mathbf{q}, jj')$$

$$- \sum_{\gamma\delta'=1}^{3}\sum_{k,k'=1}^{N_a} \Phi^{(01)}_{V,\gamma}(\mathbf{q}, jk)A_{\gamma\delta}(\mathbf{q}, kk')\Phi^{*(01)}_{V,\delta}(\mathbf{q}, k'j'),$$

$$D^{\alpha\beta}_{RR}(\mathbf{q}, jj') = \Phi^{(00)}_{RR}(\mathbf{q}, jj') \quad (13)$$

$$\times \sum_{\gamma\delta=1}^{3} \mathbf{P}^{(2)}_{j,\gamma\delta}(\Phi^{(20)}_{RR,\gamma\delta\alpha\beta}(\mathbf{q}, jj') - C^{(4)}_{\gamma\delta\alpha\beta}(\mathbf{q}, jj'))Z_j$$

$$- \sum_{\gamma\delta=1}^{3}\sum_{k,k'=1}^{N_a}\left[Z_k(\Phi^{(01)}_{R,\alpha\gamma}(\mathbf{q}, jk) - C^{(2)}_{\alpha\gamma}(\mathbf{q}, jk))\right.$$

$$\left. - \sum_{\gamma'\delta'=1}^{3} \mathbf{P}^{(2)}_{j,\gamma'\delta'}(\Phi^{(21)}_{R,\alpha}(\mathbf{q}, jk) - C^{(4)}_{\gamma'\delta'\alpha\beta}(\mathbf{q}, jk))Z_j\right]$$

$$\times A_{\gamma\delta}(\mathbf{q}, kk')\left[(\Phi^{*(01)}_{R,\delta\beta}(\mathbf{q}, k'j') - C^{(2)}_{\beta\delta}(\mathbf{q}, k'j'))Z_{k'}\right.$$

$$\left. - \sum_{\gamma'\delta'=1}^{3} \mathbf{P}^{(2)}_{j,\gamma'\delta'}(\Phi^{(21)}_{R,\beta}(\mathbf{q}, k'j') - C^{(4)}_{\gamma'\delta'\beta\alpha}(\mathbf{q}, k'j'))Z_j\right],$$

$$\mathbf{P}^{(2)}_{i,\alpha\beta} = -\frac{1}{6}\sum_{j=1}^{N_a}\sum_{\gamma\delta=1}^{3} \tilde{B}^{\alpha\beta,\gamma\delta}_{ij}$$

$$\times \sum_{k=1}^{N_a} (\Phi^{(20)}_{jk,\gamma\delta}(V_i, V_j, \mathbf{R}_{ij}) - C^{(1)}_{jk,\gamma\delta}Z_k),$$

$$\tilde{B}^{\alpha\beta,\gamma\delta}_{ij} = \left[\frac{\delta_{\alpha\beta}\delta_{ij}\delta_{\gamma\delta}}{\alpha_{Q,i}} + \Phi^{(22)}_{ij,\alpha\beta\gamma\delta}(V_i, V_j, \mathbf{R}_{ij}) - C^{(4)}_{ij,\alpha\beta\gamma\delta}\right]^{-1},$$

where N_a is the number of atoms in a unit cell and the lattice sum matrices $C^{(2)}$ and $C^{(4)}$ describe the contributions from long-range Coulomb interactions to the dynamic matrix. The short-range interaction contributions can be cast as

$$\Phi^{(ll')}_{RR,\alpha\beta}(\mathbf{q}, jj') = \sum_n \frac{\partial^2\Phi^{(ll')}\binom{n0}{jj'}}{\partial R_\alpha\binom{n}{j}\partial R_\beta\binom{0}{j'}}\exp(-i\mathbf{q}\mathbf{n}),$$

$$\Phi^{(ll')}_{VV}(\mathbf{q}, jj') = \sum_n \frac{\partial^2\Phi^{(ll')}\binom{n0}{jj'}}{\partial V_j\partial V_{j'}}\exp(-i\mathbf{q}\mathbf{n}),$$

$$\Phi^{(ll')}_{RV,\alpha}(\mathbf{q}, jj') = \sum_n \frac{\partial^2\Phi^{(ll')}\binom{n0}{jj'}}{\partial R_\alpha\binom{n}{j}\partial V_{j'}}\exp(-i\mathbf{q}\mathbf{n}), \quad (14)$$

$$\Phi^{(ll')}_{R,\alpha\beta}(\mathbf{q}, jj') = \sum_n \frac{\partial\Phi^{(ll')}\binom{n0}{jj'}}{\partial R_\beta\binom{n}{j}}\exp(-i\mathbf{q}\mathbf{n}),$$

$$\Phi^{(ll')}_{V,\alpha}(\mathbf{q}, jj') = \sum_n \frac{\partial\Phi^{(ll')}\binom{n0}{jj'}}{\partial V_{j'}}\exp(-i\mathbf{q}\mathbf{n}).$$

Note that this approach to calculating the frequencies and eigenvectors of lattice vibrations differs somewhat from the method proposed in [8], where the Gordon–Kim model was used to determine the Born–Mayer potential coefficients.

Table 2. Vibration frequencies in the hexagonal phase (in cm^{-1})

Vibration mode	Calc.	Data from [8]	Exp.	Vibration mode	Calc.	Data from [8]	Exp.
A_{1g}	52	40	55	E_{1g}	25	44	
A_{1g}	90	161		E_{1g}	53	120	55
A_{1g}	114	254	138	E_{1g}	69	157	80?
A_{1g}	149	339	178	E_{1g}	97	171	111
A_{1g}	189	368	260	E_{1g}	155	301	153
A_{1u}	*87i*	*20i*		E_{1g}	*65i*	*51i*	
A_{2g}	61	63		$E_{1u}(LO/TO)$	*49i/73i*	40	
A_{2g}	*85i*	71		$E_{1u}(LO/TO)$	0/0	0	
$A_{2u}(LO/TO)$	0/0	0		$E_{1u}(LO/TO)$	50/15	56	
$A_{2u}(LO/TO)$	42/36	35		$E_{1u}(LO/TO)$	53/51	64	
$A_{2u}(LO/TO)$	73/59	56		$E_{1u}(LO/TO)$	74/69	119	
$A_{2u}(LO/TO)$	86/83	146		$E_{1u}(LO/TO)$	98/80	171	
$A_{2u}(LO/TO)$	141/88	202		$E_{1u}(LO/TO)$	111/104	242	
$A_{2u}(LO/TO)$	157/144	271		$E_{1u}(LO/TO)$	136/128	244	
$A_{2u}(LO/TO)$	200/187	352		$E_{1u}(LO/TO)$	186/163	330	
B_{1g}	30	26		E_{2g}	24	39	
B_{1g}	70	62		E_{2g}	42	55	49
B_{1g}	77	99		E_{2g}	53	80	60
B_{1g}	83	174		E_{2g}	76	143	78
B_{1g}	155	296		E_{2g}	90	216	154
B_{1g}	185	356		E_{2g}	105	242	174
B_{1u}	61	74		E_{2g}	157	306	218
B_{1u}	*88i*	*44i*		E_{2g}	*67i*	*39i*	
B_{2g}	*84i*	*53i*		E_{2u}	*86i*	*7*	
B_{2u}	52	53		E_{2u}	27	42	
B_{2u}	57	112		E_{2u}	32	82	
B_{2u}	114	221		E_{2u}	80	135	
B_{2u}	148	276		E_{2u}	95	166	
B_{2u}	150	339		E_{2u}	119	215	
B_{2u}	202	391		E_{2u}	163	328	

To make a symmetry analysis of the eigenvectors of the normal lattice vibration modes obtained by diagonalizing the dynamic matrix (12), we made use of the projection operators to expand the eigenvectors in terms of a set of basis functions for irreducible representations of the crystal symmetry group. We constructed a complete vibrational representation $P(g)$ for the space group of the hexagonal phase and used it to calculate the projection operators [16]:

$$P_\rho = \frac{d(\rho)}{N(g)} \sum_{g \in G} \chi_\rho(g) P(g), \qquad (15)$$

where $d(\rho)$ is the dimension of a representation ρ of a point symmetry operation, $N(g)$ is the dimension of the symmetry group, $\chi_\rho(g)$ is the character of the matrix of the irreducible representation ρ, $P(g)$ is the vibrational representation of the symmetry operation of the given irreducible representation ρ of group G, P_ρ is the projection operator, and summation is performed over all symmetry group operations. An eigenvector $\mathbf{f}$ of vibration transforms according to the irreducible representation ρ of group G provided it satisfies the criterion [16]

$$P_\rho \mathbf{f} = \frac{N(g)}{d(\rho)} \mathbf{f}. \qquad (16)$$

This algorithm of expansion of the dynamic matrix eigenvectors in terms of irreducible representations was realized with the Mathematica 4.2 software package.

Table 3. Eigenvectors of fully symmetric lattice vibrations in the hexagonal phase

Atom	Coordinate	Frequency (cm^{-1})					Atom	Coordinate	Frequency (cm^{-1})				
		52	91	114	149	189			52	91	114	149	189
Rb	*X*	0.000	0.000	0.000	0.000	0.000	Cl	*X*	0.012	−0.016	0.024	−0.006	0.004
	Y	0.000	0.002	0.000	0.000	0.000		*Y*	0.012	−0.016	0.024	−0.006	0.004
	Z	0.000	0.000	0.000	0.000	0.000		*Z*	0.000	0.000	0.000	0.000	0.000
Rb	*X*	−0.001	0.000	0.000	0.000	0.000	Cl	*X*	−0.012	0.013	−0.024	0.006	−0.004
	Y	0.000	0.000	0.000	0.000	0.000		*Y*	0.000	0.000	0.000	0.000	0.000
	Z	0.000	0.000	0.000	0.000	0.000		*Z*	0.000	0.000	0.000	0.000	0.000
Rb	*X*	0.000	0.000	0.000	0.000	0.000	Cl	*X*	0.000	0.000	0.000	0.000	0.000
	Y	0.000	0.000	0.000	0.000	0.000		*Y*	−0.012	0.006	−0.024	0.006	−0.004
	Z	−0.012	0.001	0.005	−0.003	0.001		*Z*	0.000	0.000	0.000	0.000	0.000
Rb	*X*	0.000	0.000	0.000	0.000	0.000	Cl	*X*	−0.003	−0.005	−0.002	0.010	0.018
	Y	0.000	0.000	0.000	0.000	0.000		*Y*	−0.002	−0.005	−0.002	0.010	0.018
	Z	0.012	−0.001	−0.006	0.003	−0.001		*Z*	0.002	0.007	0.002	−0.001	0.003
Rb	*X*	0.000	0.000	0.000	0.000	0.000	Cl	*X*	0.003	0.005	0.002	−0.009	−0.019
	Y	0.000	0.000	0.000	0.000	0.000		*Y*	0.000	−0.001	0.000	0.000	0.000
	Z	−0.012	0.001	0.006	−0.003	0.001		*Z*	0.002	0.007	0.002	−0.001	0.003
Rb	*X*	0.000	0.000	0.000	0.000	0.000	Cl	*X*	0.000	−0.001	0.000	0.000	0.000
	Y	0.000	0.000	0.000	0.000	0.000		*Y*	0.002	0.002	0.002	−0.010	−0.018
	Z	0.012	−0.001	−0.005	0.003	−0.001		*Z*	0.002	0.007	0.002	−0.001	0.003
Mn	*X*	0.000	0.000	0.000	0.000	0.000	Cl	*X*	0.003	0.005	0.002	−0.009	−0.019
	Y	0.000	0.000	0.000	0.000	0.000		*Y*	0.002	0.006	0.002	−0.009	−0.019
	Z	0.000	0.000	0.000	0.000	0.000		*Z*	−0.002	−0.007	−0.002	0.001	−0.003
Mn	*X*	0.000	0.000	0.000	0.000	0.000	Cl	*X*	−0.003	−0.005	−0.002	0.010	0.018
	Y	0.000	0.000	0.000	0.000	0.000		*Y*	0.000	0.000	0.000	0.000	0.000
	Z	0.000	0.000	0.000	0.000	0.000		*Z*	−0.002	−0.007	−0.002	0.001	−0.003
Mn	*X*	0.000	0.001	0.000	0.000	0.000	Cl	*X*	0.000	−0.001	0.000	0.000	0.000
	Y	0.000	−0.005	0.000	0.000	0.000		*Y*	−0.002	−0.003	−0.002	0.010	0.018
	Z	−0.001	0.003	0.006	0.011	−0.005		*Z*	−0.002	−0.007	−0.002	0.001	−0.003
Mn	*X*	0.000	0.001	0.000	0.000	0.000	Cl	*X*	0.003	0.005	0.002	−0.009	−0.019
	Y	0.000	0.006	0.000	0.000	0.000		*Y*	0.002	0.006	0.002	−0.000	−0.019
	Z	0.001	−0.003	−0.005	−0.011	0.005		*Z*	0.002	0.007	0.002	−0.001	0.003
Mn	*X*	0.000	0.001	0.000	0.000	0.000	Cl	*X*	−0.003	−0.005	−0.002	0.010	0.018
	Y	0.000	0.006	0.000	0.000	0.000		*Y*	0.000	0.000	0.000	0.000	0.000
	Z	−0.001	0.003	0.005	0.011	−0.005		*Z*	0.002	0.007	0.002	−0.001	0.003
Mn	*X*	0.000	0.001	0.000	0.000	0.000	Cl	*X*	0.000	−0.001	0.000	0.000	0.000
	Y	0.000	−0.005	0.000	0.000	0.000		*Y*	−0.002	−0.003	−0.002	0.010	0.018
	Z	0.001	−0.003	−0.006	−0.011	0.005		*Z*	0.002	0.007	0.002	−0.001	0.003
Cl	*X*	−0.012	0.013	−0.025	0.006	−0.004	Cl	*X*	−0.003	−0.005	−0.002	0.010	0.018
	Y	−0.012	0.013	−0.025	0.006	−0.004		*Y*	−0.002	−0.005	−0.002	0.010	0.018
	Z	0.000	0.000	0.000	0.000	0.000		*Z*	−0.002	−0.007	−0.002	0.001	−0.003
Cl	*X*	0.012	−0.016	0.024	−0.006	0.004	Cl	*X*	0.003	0.005	0.002	−0.009	−0.019
	Y	0.000	0.001	0.000	0.000	0.000		*Y*	0.000	−0.001	0.000	0.000	0.000
	Z	0.000	0.000	0.000	0.000	0.000		*Z*	−0.002	−0.007	−0.002	0.001	−0.003
Cl	*X*	0.000	0.000	0.000	0.000	0.000	Cl	*X*	0.000	−0.001	0.000	0.000	0.000
	Y	0.012	−0.006	0.025	−0.006	0.004		*Y*	0.002	0.002	0.002	−0.010	−0.018
	Z	0.000	0.000	0.000	0.000	0.000		*Z*	−0.002	−0.007	−0.002	0.001	−0.003

5. RESULTS AND DISCUSSION

The results of the calculations of the eigenfrequencies and their assignment according to irreducible representations of the crystal symmetry group are compared in Table 2 with the results quoted in [8] and the frequencies of the experimentally observed Raman spectral lines; the eigenvectors of the fully symmetric (A_{1g}) vibrations are presented in Table 3.

The calculated and experimental frequencies for all vibration modes are seen to be in satisfactory agreement considering that the method of calculation did not employ fitting parameters. Some of the calculated frequencies turned out to be imaginary, which indicates the lattice of the hexagonal phase to be unstable at 0 K and is in accord with the phase transition in $RbMnCl_3$ observed to occur at 272 K [3] (a comprehensive analysis of the origin of this instability is given in [8] in terms of a similar approach; we do not dwell on it here). We did not succeed in observing the lowest frequency modes near 20 cm^{-1}, apparently because of the low-frequency dynamics undergoing strong rearrangement at this phase transition; this could also be associated, however, with the strong wing of Rayleigh scattering in this region. In accordance with experiment, the calculation shows that the highest frequency vibrations correspond to the irreducible representation A_{1g}; an analysis of their eigenvectors (Table 3) suggests that such vibrations are primarily connected with the chlorine ions being displaced in the Mn–Cl bond direction (although they also have a small contribution from the manganese ions and even an insignificant contribution from the heavy rubidium ions). As seen from Table 2, the disagreement between the calculated and experimental frequencies is the largest in this spectral region.

In the middle frequency range, the agreement between the calculated and experimental frequencies is noticeably better; the dynamics is governed here apparently primarily by long-range Coulomb interactions of the ions. Interestingly, the heavy rubidium ions provide a substantial contribution to the eigenvectors of the fairly high-frequency modes at 114 and 149 cm^{-1}, which is even larger than that to the lower lying modes (Table 3).

Note that the calculation of the crystal lattice potential and of the phonon spectrum performed in [8] took into account only the Coulomb interaction of point ions and the short-range repulsion of spherically symmetric free ions. However, as shown in [7], the energetically preferable structure for $RbMnCl_3$ in this case is cubic rather than hexagonal. Stabilization of the latter structure is determined by the polarization energy, which is connected with the presence of dipole and quadrupole ion moments.

Note, however, that the frequency spectra obtained by the methods used in [7] and [8] are qualitatively similar; also similar are the numbers of imaginary frequencies corresponding to vibrations that are unstable at low temperatures (the lowest positive frequency of 7 cm^{-1}, which was obtained with the Born–Mayer potential, turned out to be imaginary when the multipole distortions of the electronic density were included). This similarity suggests that an analysis of the origin of the lattice instability at low temperatures (which is determined primarily by the low-frequency dynamics) should yield similar results in both cases. Good qualitative agreement is also observed in the middle frequency range (up to 50–60 cm^{-1}). By contrast, in the region of high-frequency vibrations, which are associated primarily with the stretch vibrations of the Mn–Cl bonds, the results are in obvious disagreement. Apparently, this indicates overestimation of the force constants of these bonds with the Born–Mayer potential, whereas the multipole approximation underestimates them.

The agreement between the calculated (1.1 GPa) and experimental (0.7 GPa) pressures for the transition from the hexagonal to cubic phase should apparently be considered satisfactory. This is corroborated by the optical isotropy of the crystal and the absence of Raman scattering. Note that this phase transition, associated with a considerable rearrangement of the lattice, entails separation of the phases that coexist in the pressure interval 0.4–0.8 GPa (and, possibly, at still higher pressures near the sample surface, where structural defects should play an appreciable role).

6. CONCLUSIONS

Thus, our study has revealed that the fitting parameter–free method proposed in [8, 15] permits efficient calculation of the lattice stability and dynamics of ionic crystals in fairly complex structures. A comparative analysis of Raman scattering and of the calculated lattice vibration spectrum for the $RbMnCl_3$ hexagonal phase made it possible to assign most of the Raman lines allowed by the selection rules and to determine the eigenvectors of the corresponding vibrations. Some differences between the experimental and calculated frequencies observed in the high-frequency part of the spectrum can be tentatively related to the covalency of the Mn–Cl bonds.

The pressure-induced transition from the hexagonal to cubic phase, which was earlier observed to occur only at high temperatures, has been detected at room temperature, in full agreement with calculations [5]. This transition takes place through separation of the phases that coexist in the range 0.4–0.8 GPa, which correlates with the calculated pressure of 1.1 GPa at which the hexagonal phase becomes unstable; the phase transition was found to be reversible and was not accompanied by noticeable hysteresis effects. A further increase in pressure was observed to drive transitions at 1.1 GPa and, tentatively, at 5 GPa.

ACKNOWLEDGMENTS

The authors are indebted to K.S. Aleksandrov for helpful discussions and to A.P. Shebanin for assistance in performing the spectral measurements under pressure.

This study was supported jointly by the Russian Foundation for Basic Research and Krasnoyarsk Science Foundation Eniseĭ (project no. 02-02-97707) and the program of the Siberian Division of the Russian Academy of Sciences "Integration" (project no. 88).

REFERENCES

1. K. S. Aleksandrov, A. T. Anistratov, B. V. Beznosikov, and N. V. Fedoseeva, *Phase Transitions in Crystals of ABX_3 Haloid Compounds* (Nauka, Novosibirsk, 1981).
2. K. S. Aleksandrov and B. V. Beznosikov, *Perovskite-like Crystals* (Nauka, Novosibirsk, 1999).
3. K. S. Aleksandrov, A. T. Anistratov, S. V. Mel'nikova, V. I. Zinenko, L. A. Shabanova, and A. D. Shefer, Fiz. Tverd. Tela (Leningrad) **21**, 1119 (1979) [Sov. Phys. Solid State **21**, 650 (1979)].
4. J. M. Longo and J. A. Kafalas, J. Solid State Chem. **3**, 429 (1971).
5. I. P. Aleksandrova, V. F. Shabanov, A. K. Moskalev, *et al.*, *Structural Phase Transitions in Crystals at High Pressure* (Nauka, Novosibirsk, 1982).
6. V. I. Zinenko, N. G. Zamkova, and S. N. Sofronova, Zh. Éksp. Teor. Fiz. **123**, 846 (2003) [JETP **96**, 747 (2003)].
7. V. I. Zinenko, N. G. Zamkova, and S. N. Sofronova, Zh. Éksp. Teor. Fiz. **114**, 1742 (1998) [JETP **87**, 944 (1998)].
8. M. B. Smirnov and V. Yu. Kazimirov, Kristallografiya **48**, 480 (2003) [Crystallogr. Rep. **48**, 435 (2003)].
9. J. Goodyear, G. A. Steigmann, and E. M. Ali, Acta Crystallogr. B **33**, 256 (1977).
10. A. S. Krylov, A. D. Shefer, and A. N. Vtyurin, Prib. Tekh. Éksp., No. 3, 146 (1995).
11. Q. Wang, G. Ripault, and A. Bulou, Phase Transit. **53**, 1 (1995).
12. S. V. Goryainov and I. A. Belitsky, Phys. Chem. Miner. **22**, 443 (1995).
13. R. G. Munro, G. J. Piermarini, S. Block, and W. B. Holzapfel, J. Appl. Phys. **57**, 165 (1985).
14. K. S. Aleksandrov, V. N. Voronov, A. N. Vtyurin, S. V. Goryaĭnov, N. G. Zamkova, V. I. Zinenko, and A. S. Krylov, Zh. Éksp. Teor. Fiz. **121**, 1239 (2002) [JETP **94**, 977 (2002)].
15. O. V. Ivanov and E. G. Maksimov, Zh. Éksp. Teor. Fiz. **108**, 1841 (1995) [JETP **81**, 1008 (1995)].
16. H. Streitwolf, *Gruppentheorie in der Festkörperphysik* (Teubner, Leipzig, 1967; Mir, Moscow, 1971).

Translated by G. Skrebtsov